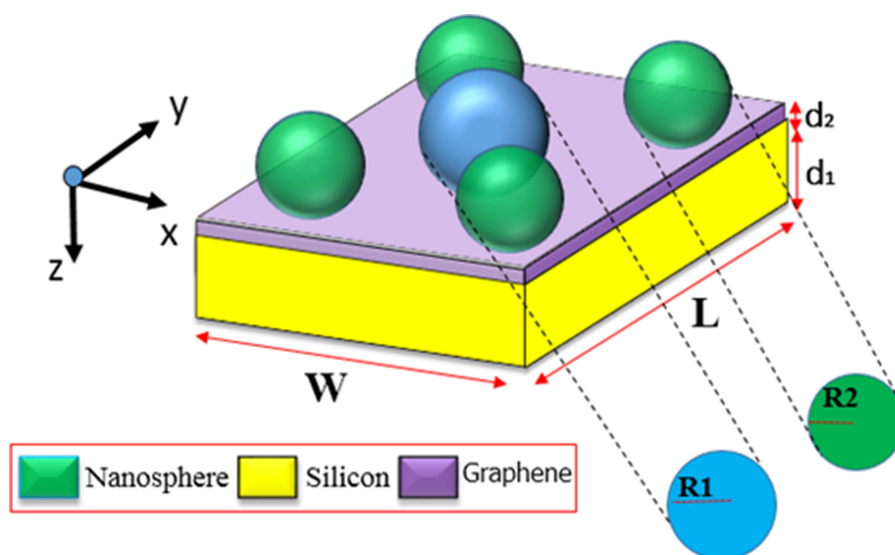


Tunable Plasmon Induced Transparency in Graphene and Hyperbolic Metamaterial-Based Structure





Volume 11, Number 4, August 2019

Muhammad Abuzar Baqir
Pankaj Kumar Choudhury, *Senior Member, IEEE*
Ali Farmani, *Member, IEEE*
T. Younas
J. Arshad
Ali Mir, *Member, IEEE*
S. Karimi, *Member, IEEE*



DOI: 10.1109/JPHOT.2019.2931586

Tunable Plasmon Induced Transparency in Graphene and Hyperbolic Metamaterial-Based Structure

Muhammad Abuzar Baqir ¹,
Pankaj Kumar Choudhury ², *Senior Member, IEEE*,
Ali Farmani ³, *Member, IEEE*, T. Younas,¹ J. Arshad,¹
Ali Mir ³, *Member, IEEE*, and S. Karimi,³ *Member, IEEE*

¹Department of Electrical and Computer Engineering, COMSATS University Islamabad, Sahiwal 57000, Pakistan

²Institute of Microengineering and Nanoelectronics, Universiti Kebangsaan Malaysia, Selangor 43600, Malaysia

³Department of Electrical Engineering, Lorestan University, Lorestan 68151-44316, Iran

DOI:10.1109/JPHOT.2019.2931586

This work is licensed under a Creative Commons Attribution 4.0 License. For more information, see <https://creativecommons.org/licenses/by/4.0/>

Manuscript received July 11, 2019; accepted July 24, 2019. Date of publication July 29, 2019; date of current version August 12, 2019. The work of M. A. Baqir was supported in part by the Higher Education Commission (Pakistan) under Grant 21-1811/SRGP/R&D/HEC/2017. The work of P. K. Choudhury was supported in part by the Ministry of Higher Education (MOHE, Malaysia) through Grant AKU254 under the HiCOE (Fasa II). Corresponding author: Pankaj Kumar Choudhury (e-mail: pankaj@ukm.edu.my).

Abstract: A specially designed tunable hyperbolic metamaterial (HMM) based on plasmon induced transparency (PIT) of fractal in the near-infrared (NIR) regime was proposed. The HMM-layer constitutes the top metasurface, which is comprised of fractal-like nanospheres of silver (Ag) metal. A bilayer of graphene is sandwiched between the top HMM and bottom silicon (Si) substrate. The permittivity of graphene bilayer was deduced corresponding to different chemical potentials (of graphene). PIT of the proposed structure was obtained in the 3000–4000 nm wavelength band by employing the finite difference time domain simulation under the excitation of a fundamental transverse magnetic (TM) mode. The effects of incidence angle and graphene chemical potential on the transmission characteristics were investigated. Furthermore, the PIT windows could be tuned by altering the radii of Ag nanospheres in the HMM layer and chemical potential of bilayer graphene. Such systems would be useful in varieties of applications, e.g., switching, energy harvesting, sensing in environmental, and/or medical diagnostics, particularly in detecting the existing impurities in human blood and urine.

Index Terms: Plasmon induced transparency, graphene, metamaterials.

1. Introduction

The phenomenon of surface plasmon polariton (SPP) waves propagating along the metal-dielectric interface can be effectively exploited to devise varieties of optical components, namely sensors, absorbers, filters, perfect lenses, slow-light memory devices, etc. [1]–[7]. This essentially becomes possible owing to the surface plasmon resonance (SPR) condition being highly responsive to the light-matter interaction, which is precisely governed by the shape, size and type of medium along with the operating conditions. The magnetic response of specially designed metamaterials due to the occurrence of SPP has also been reported in the literature [8]–[9] with the emphasis on the effect of tailoring the SPP waves by altering the configuration of metasurface.

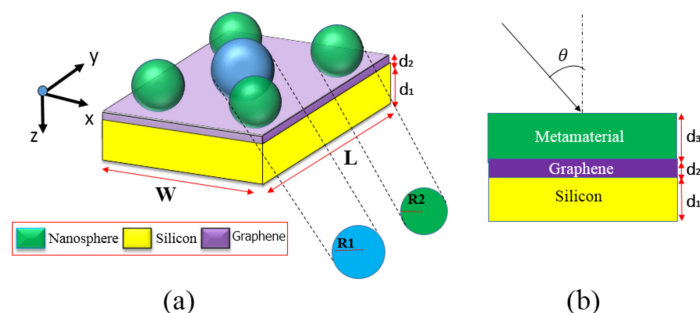


Fig. 1. Schematic of the PIT metamaterial structure; (a) 3D unit cell and (b) 2D representation of schematic.

Within the context, plasmon induced transparency (PIT) is the quantum-interference effect of electromagnetic (EM) induced transparency (EIT) in laser stimulated nuclear architectures [10]. The phenomenon induces sharp transmittance in a wide range of absorption spectrum [11], and remains prudent in various slow-light applications [12] and improvements in non-linear effect [13]. Also, PIT is extensively used in metamaterial-based configurations, because the geometrical parameters of these can be altered, in order to achieve PIT tuning for *on-demand* kind of applications. This makes dynamically tunable PIT to be in practice [14]. Reference [15] demonstrates the use of hybrid metal-graphene metamaterial structure to attain control over broadband PIT in the THz regime. In this work, the unit cell is comprised of cut wire, mono-layer graphene sheets and four U-shaped resonators; the broadband PIT is achieved with near-field coupling via destructive interference.

Graphene mediums, being attractive in photoelectric modulation [16]–[17] owing to their ability to change the surface conductivity and fast response time (in picoseconds), are greatly useful in many optical applications, viz. ultra-fast switching, absorbers, slow-light propagation etc. [18]–[21]. Propagation of graphene plasmons can be controlled by modulating the external electrical field, and also, the environmental temperature. It has been shown that strong coupling between the incident waves and the graphene plasmons can yield the ways to realize optical switching [22]. Zeng *et al.* experimentally demonstrated frequency-tunable ultra-high speed intensity modulation in the mid-infrared regime exploiting hybrid graphene metasurface [23]. Reference [24] discusses a tunable transparent position PIT by using nanoengineered graphene-based metamaterial. In refs. [25]–[26], the authors describe PIT in the THz regime of EM spectrum by using graphene complementary metamaterials. Also, hybrid metal-graphene metamaterials are used to control the amplitude of transparency window of narrowband PIT [27].

The previously reported research results determine the observation of PIT from metasurface structures with broken symmetry [28]–[29] and defects [30]–[31]. This essentially motivates the need for appropriate photo modulation scheme with extra degrees of freedom, which would be feasible with the advancements of photonic nanostructure fabrication technology. With this viewpoint in mind, the present paper aims to investigate PIT exploiting metasurface comprised of fractal-like structure. More specifically, we consider the silver (Ag) nanosphere-graphene-dielectric kind of combination as the illustrative case, and analyze the spectral characteristics under finite difference time domain (FDTD) simulations, assuming various parametric and operational conditions. In this stream, we take different values of volume fraction element (of Ag nanosphere in the metasurface), angle of incidence and chemical potential of graphene, and emphasize the characteristic spectral features of PIT, assuming the incidence excitation to be TM-polarized. The wavelength-dependence of effective permittivity (of metasurface) is also determined.

2. Model and Theory

Figure 1 shows the schematic of the proposed hyperbolic metamaterial (HMM)-based configuration, which is composed of three layers – the top metasurface, bottom silicon (Si) layer, and a graphene

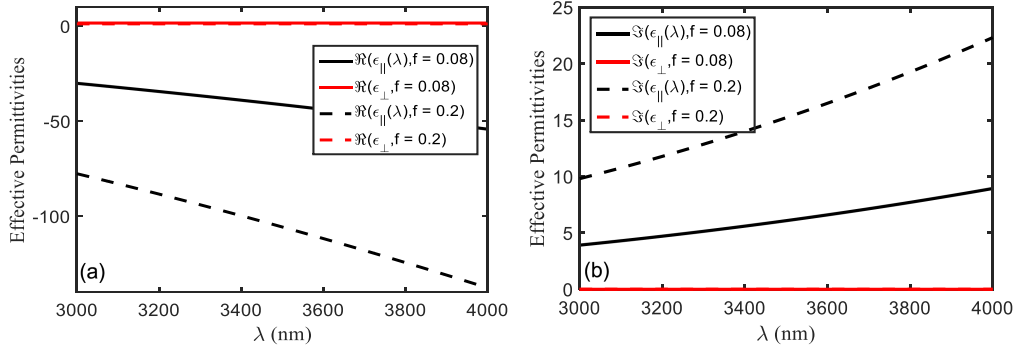


Fig. 2. Wavelength-dependence of (a) real and (b) imaginary parts of effective permittivity (of the HMM layer) for the values of f as 0.08 and 0.2.

bilayer as sandwiched between the two. Figure 1a illustrates the schematic of the unit cell of PIT structure, whereas Fig. 1b depicts the 2D view of the configuration. As becomes clear from Fig. 1a, the metasurface is comprised of fractal-like Ag nanospheres of two different radii R_1 and R_2 that correspond to the features of central and surrounding nanospheres, respectively. Also, the unit cell structure has the dimension as $0.2 \times 0.2 \mu\text{m}^2 \times (d_1 + d_2 + d_3)$ nm. The transmission characteristics of this configuration are obtained by simulating the metamaterial in FDTD by employing the periodic boundary conditions along the xy -plane. However, the perfectly-matched layer (PML) boundary condition is applied above the excitation source and below the transmission monitor.

We now obtain the effective permittivity of metasurface by exploiting the effective medium theory [32]. As stated before, we consider the top metasurface as a layered medium comprised of periodically arranged thin Ag nanosphere. The parallel and perpendicular components of effective permittivity (of metasurface) can be written as

$$\epsilon_{\parallel}(\lambda) = \epsilon_d \frac{(1+f)\epsilon_m(\lambda) + (1-f)\epsilon_d}{(1-f)\epsilon_m(\lambda) + (1+f)\epsilon_d} \quad (1a)$$

and

$$\epsilon_{\perp}(\lambda) = f\epsilon_m(\lambda) + (1-f)\epsilon_d, \quad (1b)$$

respectively. Here f is the volume fraction element (or fill-factor) of Ag metal in the unit cell of metasurface, $\epsilon_m(\lambda)$ is the wavelength-dependent permittivity, and ϵ_d is the dielectric permittivity, which is free-space (with $\epsilon_d = 1$) in the present case.

Now, we deduce the longitudinal and transverse components of effective permittivity by employing Eq. (1). Since silver is dispersive in nature, its wavelength-dependent permittivity can be obtained by using the Lorentz-Drude model [33] that provides the best approximation of dielectric constant with the experimental results; it is given as

$$\epsilon_m(\omega) = 1 - \frac{f_1 \omega_p^2}{\omega(\omega - j\Gamma_1)} + \sum_n \frac{f_n \omega_p^2}{\omega_n^2 - \omega^2 + j\omega\Gamma'_n} \quad (2)$$

In this equation, f_1 and f_n are oscillator strengths, ω_p is plasma frequency, Γ_1 is damping constant, and ω'_n and Γ'_n are oscillator frequency and bandwidth, respectively. Also, ω is the operating angular frequency. As silver is nonmagnetic in nature at optical frequencies, we take its permeability to be $\mu_{ds} = 1$.

We now attempt to observe the wavelength-dependence of effective permittivity considering two illustrative values of fill-factor f , namely 0.08 and 0.2; Fig. 2 illustrates the respective plots. Here Fig. 2a shows the plots of the real (\Re) part of effective permittivity against wavelength λ , whereas Fig. 2b depicts the λ -dependence of the imaginary (\Im) part of the same. We observe that, for the chosen values of fill-factor, the real parts of parallel component ϵ_{\parallel} of effective permittivity remain negative, whereas the imaginary parts of ϵ_{\parallel} are positive. With the increase in the value of f , the

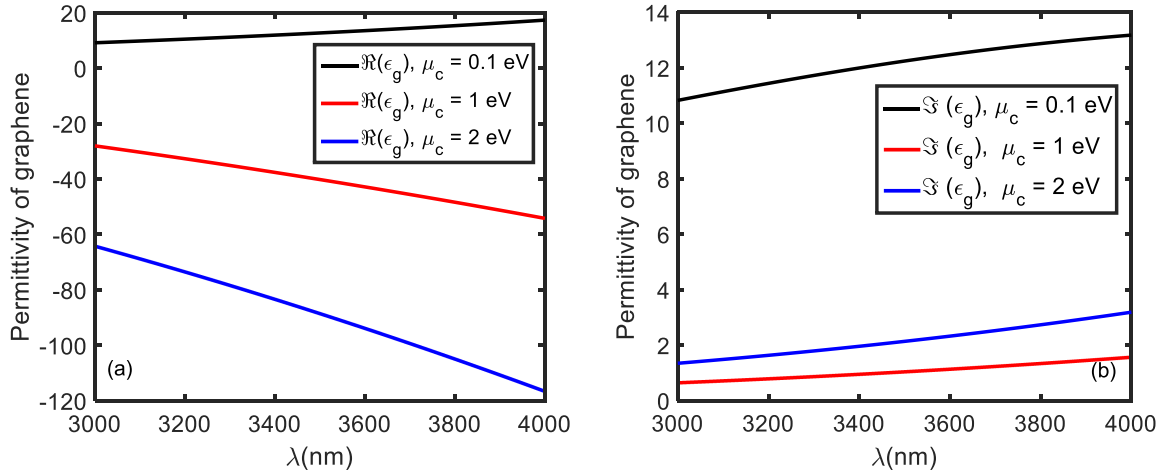


Fig. 3. Wavelength-dependence of the (a) real and (b) imaginary parts of bilayer graphene permittivity corresponding to different chemical potentials.

$\Re(\epsilon_{\parallel})$ part becomes more negative, and $\Im(\epsilon_{\parallel})$ becomes more positive. Further, with the increase in operating wavelength λ , $\Re(\epsilon_{\parallel})$ attains more negative values, whereas $\Im(\epsilon_{\parallel})$ tends to be more positive. Interestingly, for the chosen values of f , both the real and imaginary parts of the perpendicular component ϵ_{\perp} of effective permittivity become vanishing, and also, remain independent of wavelength. A null-valued imaginary part of effective permittivity essentially makes the medium to be non-absorptive in nature, and therefore, the choice of $f = 0.08$ allows the metasurface to be highly transparent in the 3000–4000 nm span of operating wavelength.

The permittivity of graphene bilayer can be analyzed for different values of chemical potential in the stated wavelength band of interest, i.e., 3000–4000 nm. In this stream, the conductivity of graphene can be deduced by Kabou equation [34]–[35]. The complex-valued surface conductivity $\sigma_g(\omega)$ of graphene is determined by the well-established and experimentally valid theoretical model, which makes it to be the algebraic sum of the intra- and inter-band conductivities [22], i.e.,

$$\sigma_g(\omega) = \sigma_{intra}(\omega) + \sigma_{inter}(\omega) \quad (3)$$

The intra-band conductivity is due to the collective behavior of free electrons, and can be given as

$$\sigma_{intra}(\omega) = j \frac{e^2 K_B T}{\pi^2 (\omega + j\tau^{-1})} \left[\frac{\mu_c}{K_B T} + 2 \ln \left\{ \exp \left(-\frac{\mu_c}{K_B T} \right) + 1 \right\} \right] \quad (4)$$

Also, the conductivity due to the inter-band transition is approximated, following the conditions $\frac{\hbar}{2\pi}\omega \gg K_B T$, and is finally obtained as

$$\sigma_{inter}(\omega) = j \frac{e^2}{4\pi\hbar} \ln \left[\frac{2|\mu_e| - \hbar(\omega + j\tau^{-1})}{2|\mu_e| + \hbar(\omega + j\tau^{-1})} \right] \quad (5)$$

In Eqs. (4) and (5), e and τ , respectively, determine the electronic charge and momentum relaxation time. Apart from these, μ_c , K_B and T represent the chemical potential (also called as the Fermi energy E_f), Boltzmann constant and temperature, respectively.

The permittivity of graphene can be stated as [36]

$$\epsilon_g(\omega) = 1 + j \frac{\sigma_g(\omega)}{\omega \epsilon_0 \Delta} \quad (6)$$

where Δ is the thickness of graphene and ϵ_0 is the free-space permittivity.

Figure 3 depicts the wavelength-dependence of bilayer graphene permittivity corresponding to four different values of chemical potential μ_c , namely 0.1 eV, 1 eV and 2 eV, in the 3000–4000 nm

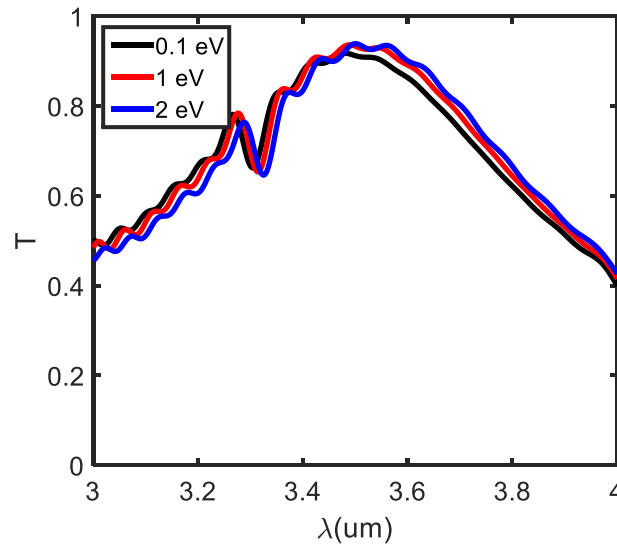


Fig. 4: Transmission spectra corresponding to different values of μ_c with $R_1 = 400$ nm and $R_2 = 200$ nm under normal incidence.

wavelength band. We consider the thickness Δ of graphene as 0.9 nm in the present case. Figure 3a corresponds to the plots of the real part $\Re(\epsilon_g)$ of permittivity against wavelength, whereas Fig. 3b illustrates the λ -dependence of the imaginary part $\Im(\epsilon_g)$. We observe in these figures that, with the increase in μ_c , the $\Re(\epsilon_g)$ part becomes more negative (Fig. 3a), whereas $\Im(\epsilon_g)$ remains positive-valued for all the chosen values of μ_c (Fig. 3b). Figure 3a shows that $\Re(\epsilon_g)$ is positive corresponding to $\mu_c = 0.1$, and it remains in the range of ~ 10 – 20 as the wavelength is varied from 3000 nm to 4000 nm. For the other values of μ_c , it becomes highly negative. For higher μ_c -values, the increase in λ also causes $\Re(\epsilon_g)$ to be more negative. On the other hand, as Fig. 3b depicts, $\Im(\epsilon_g)$ increases with the increase in λ , which becomes less prominent as the value of μ_c is increased.

3. Results and Discussion

We now investigate the PIT characteristics of the proposed metasurface configuration exploiting the FDTD simulation technique in the 3000–4000 nm wavelength band of operation. For this purpose, we consider the aforementioned three different values of chemical potential μ_c (of graphene), and the TM-polarized incidence radiation impinges the top HMM surface at the angle θ having values as 0° (i.e., the case of normal incidence), 20° and 40° . We take two different kinds of fractal-like structures (of metasurface) to simulate, depending on the radii of nanospheres – Case 1: $R_1 = 400$ nm, $R_2 = 200$ nm and Case 2: $R_1 = 500$ nm, $R_2 = 250$ nm. As such, in these two illustrative cases, we alter the dimensional features of central and surrounding nanospheres in certain proportion. We now discuss the transmission characteristics obtained in these two parametric situations individually, considering the effects of μ_c and θ , as in the following:

Case 1: Figure 4 exhibits the dependence of transmission on the operating wavelength band, when the parametric values in forming the metasurface are as $R_1 = 400$ nm, $R_2 = 200$ nm. To obtain these plots, we consider three different values of μ_c , namely 0.1 eV, 1 eV and 2 eV, and the normal incidence (i.e., $\theta = 0^\circ$) of TM-polarized waves on the top metasurface. We observe that there exist two transmission peaks corresponding to the values of λ close to 3300 nm and 3500 nm (on average) with the transmittance nearly 75% and 95%, respectively. However, some ripples exist in the transmittance patterns, which may be attributed to the partial scattering of waves by the silver nanospheres in the metasurface. We further observe that, corresponding to both the stated wavelength values, the increase in μ_c results in red-shifts in transmission peaks. Figure 4 also demonstrates that, near 3300 nm wavelength, low μ_c shows a little higher transmittance

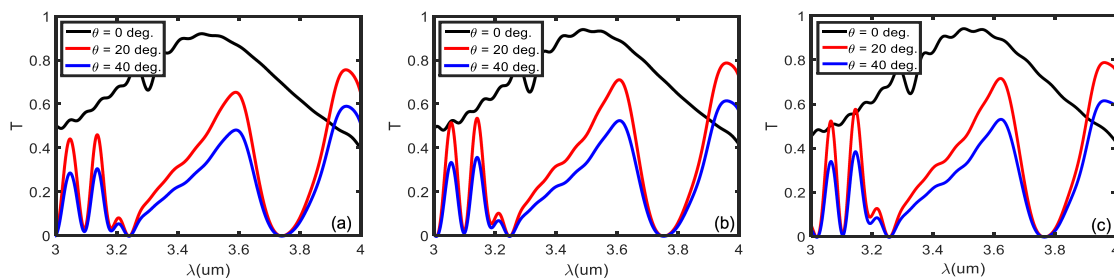


Fig. 5. Transmission spectra for different incidence angles, keeping μ_c as (a) 0.1 eV, (b) 1 eV and (c) 2 eV, when $R_1 = 400$ nm and $R_2 = 200$ nm.

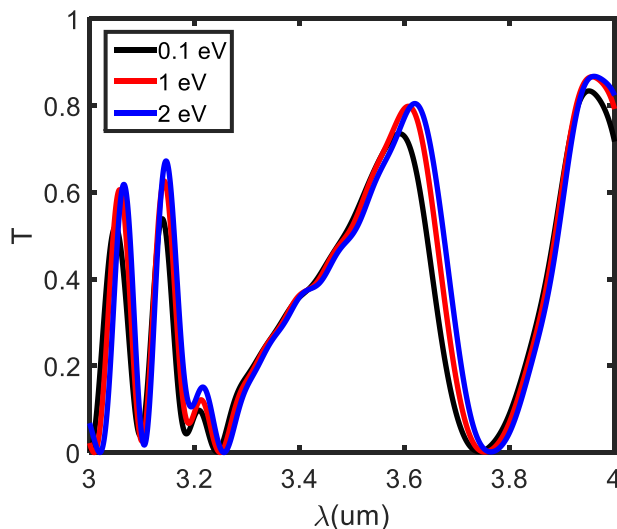


Fig. 6. Transmission spectra corresponding to different values of μ_c with $R_1 = 500$ nm and $R_2 = 250$ nm under normal incidence.

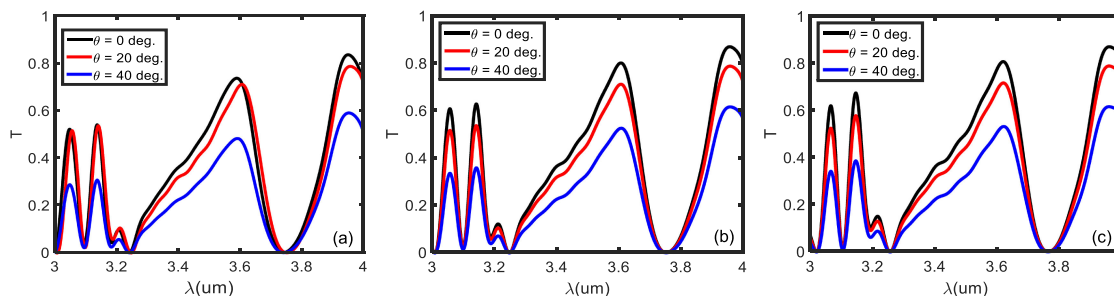


Fig. 7. Transmission spectra for different incidence angles, keeping μ_c as (a) 0.1 eV, (b) 1 eV and (c) 2 eV, when $R_1 = 500$ nm and $R_2 = 250$ nm.

than that observed for the use of high μ_c -values. However, we notice opposite behaviour near 3500 nm wavelength in terms of transmittance obtained for different μ_c -values. As such, we find that graphene Fermi energy has impact on the transmission characteristics, though it is not highly significant in the used range of λ . It is also evident from Fig. 4 that the transmission patterns are too broad, which justifies weak light-matter coupling in this case, and hence, the absence of PIT results in.

Figure 4 illustrates the case of normal incidence. In order to observe the effect of incidence angle on transmittance, we plot in Fig. 5 the wavelength-dependence of transmission, considering the

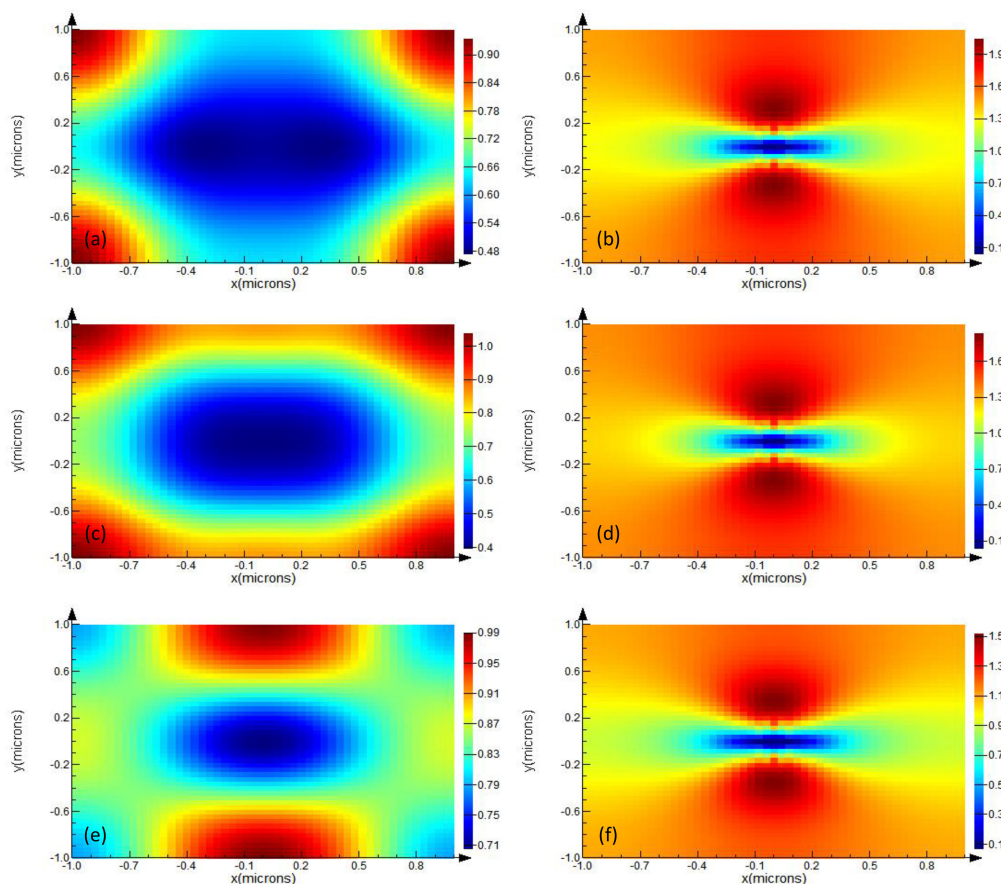


Fig. 8. Electric field distributions in the unit cell of metasurface corresponding to the PIT peaks obtained ~ 3055 nm (a, b), ~ 3145 nm (c, d), and ~ 3610 nm (e, f) when $\mu_c = 1$ eV and incidence angle θ as 20° (as obtained in Fig. 5b). Figures a, c, e correspond to the bottom-surface E-field patterns; figs. b, d, f correspond to the top-surface E-field.

oblique incidence (with θ -values as 20° and 40°) of TM-polarized incidence excitation as well, along with the normal incidence. In this stream, Figs. 5a–c represent the cases of graphene chemical potentials as 0.1 eV, 1 eV and 2 eV, respectively. We see in Fig. 5 that the oblique incidence results in PIT, and four different PIT windows exist corresponding to the λ -values nearly 3050 nm, 3150 nm, 3600 nm and 3950 nm; the transmission peaks keep increasing for larger wavelengths. As stated before, the increase of μ_c causes very small red-shifts in PIT peaks. Interestingly, changes in obliquity apparently do not introduce shifts in PIT peaks. It only affects the magnitude of transmission instead, which decreases with the increase in incidence angle. Figures 4 and 5 make it explicit that a normal incidence results in weak light-matter interaction. In contrast, the obliquity of incidence contributes to relatively stronger coupling of light with matter. The obtained PIT windows are the results of bright and dark modes coupling, and the transmittance varies from 45% to 75%. As such, we notice that the first two PIT windows have relatively high Q -factor owing to the presence of sharp peaks in spectral patterns. Within the context, the Q -factor is generally defined as $Q = f_r / FWHM$ with f_r and $FWHM$ being the resonance frequency and full-width half-maximum (of the transmission window), respectively. As such, a wider transmission window determines low Q -factor.

Case 2: Seeking the possibilities to increase transmittance, Fig. 6 exhibits the transmission spectra in the case of $R_1 = 500$ nm and $R_2 = 250$ nm in the feature of metasurface, considering the normal TM-polarized incidence excitation and μ_c -values as 0.1 eV, 1 eV and 2 eV. This figure exhibits that the coupling of light with matter becomes strong in this case, and yields four PIT windows (that

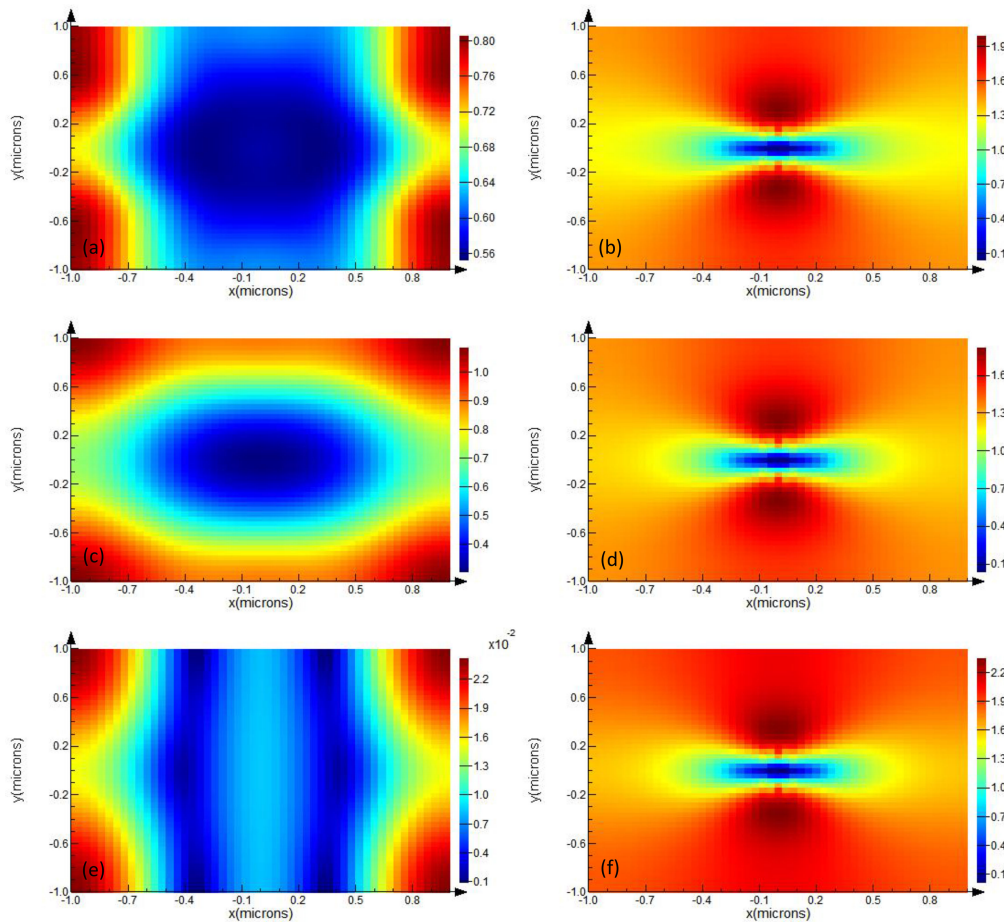


Fig. 9. Electric field distributions in the unit cell of metasurface corresponding to the PIT peaks obtained ~ 3065 nm (a, b), ~ 3145 nm (c, d), and ~ 3620 nm (e, f) when $\mu_c = 2$ eV and incidence angle θ as 20° (as obtained in Fig. 5c). Figures a, c, e correspond to the bottom-surface E-field patterns; figs. b, d, f correspond to the top-surface E-field patterns.

correspond to four bright and dark modes) with the transmittance peaks at wavelengths nearly 3050 nm, 3150 nm, 3600 nm and 3950 nm. The ripples, as observed in Fig. 4, are also almost eliminated in this case, which must be attributed to the increased fill-factor that results in reduced scattering of waves in the metasurface. Further, the transmission windows become broader with the increase in wavelength. However, those (transmission windows) are relatively sharp at low operating wavelengths, thereby indicating relatively higher Q -factor. As observed in Case 1 before, the increase in μ_c causes red-shifts in transmission peaks. Interestingly, the positions of peaks do not alter significantly (with the changes in the feature of metasurface) in this case; it is the transmittance only that becomes more pronounced now (varies from $\sim 62\%$ to 85%). As such, proportionate alterations in the dimensional features of nanospheres (in the metasurface) do not alter positions of peaks in transmission spectra.

Figure 7 depicts the wavelength-dependence of transmittance for the normal as well as oblique incidence of TM-polarized waves, considering the aforementioned chosen values of μ_c , i.e., 0.1 eV, 1 eV and 2 eV; Figs. 7a–d illustrate the respective transmission characteristics. We find the PIT properties as closely similar to what we observed in Fig. 5 representing the Case 1 for metasurface with smaller fill-factor. The only differences with larger fill factor (Fig. 7) are that the magnitudes of transmission are increased in this case, and also, the situation of normal incidence too contributes to strong field-matter interaction. Apart from these, the increase of chemical potential results in

a little larger transmittance without altering the positions of transmission peaks. The reduction in ripples in PIT spectra also suggests the use of larger fill-factor (in forming the metasurface) to be a better choice.

Electric field distributions: Figures 8 and 9, respectively, show the two-dimensional (2D) electric field distribution patterns of the unit cell in metasurface corresponding to the PIT peaks obtained in Figs. 5b and 5c for the respective values of chemical potential μ_c as 1 eV and 2 eV. As the illustrative case, we consider the peaks obtained corresponding to 20° incidence angle. Also, we plot the top and well as bottom surface E-field patterns. In all these plots, the stated dimensions in the x - and y -directions determine the size of the unit cell. Within the context, the dimensional range of simulation has been stated before in Section 2.

As we observe in Fig. 5b (corresponding to $\mu_c = 1$ eV), the positions of the first, second and third peaks appear very close to 3055 nm, 3145 nm and 3610 nm, respectively. In this figure, the first and second peaks are very sharp, whereas the third peak has relatively wider *FWHM* value. This becomes obvious in Fig. 8 as well; here Figs. 8a, c, e exhibit the bottom-surface E-field, whereas Figs. 8b, d, f illustrate the top-surface E-field patterns. In all these plots, we see that the maximum confinement of power takes place in the central portion of the unit cell.

Corresponding to the PIT related results in Fig. 5c obtained for $\mu_c = 2$ eV, we observe that the three peaks are positioned at the values of wavelengths close to 3065 nm, 3145 nm and 3620 nm. Also, the *FWHM* values of these peaks increase with the increase in wavelength. Figure 9 exhibits the bottom- (Fig. 9a, c, e) and top- (Fig. 9b, d, f) surface E-field patterns in the unit cell corresponding to the positions of peak wavelengths, which exhibit the confinement characteristics of fields in the metasurface.

4. Conclusion

The obtained results indicate that the effective permittivity of metasurface essentially depends on the fill-factor of silver in forming the metasurface. Looking at the permittivity of graphene bilayer in configuration, the real part of it becomes more negative with the increase in chemical potential (of graphene); the imaginary part, however, remains positive in all situations. The obtained PIT spectral characteristics determine that, among the two different dimensional features of silver nanospheres in forming the metasurface (or the fill-factor), the case of lower dimensional values allows PIT to occur for oblique incidence of TM polarized waves. This is very much evident from the sharp peaks in transmission spectrum corresponding to oblique incidence, thereby presenting stronger light-matter-interactions. The doubling of nanosphere dimensions in metasurface makes the PIT phenomenon to be stronger, along with increase in transparency. Further, the change in chemical potential does not alter the positions of PIT peaks; it merely contributes to small increase in transparency. As such, the results reveal *on-demand* kind of control over PIT of certain metasurface configuration through altering the obliquity of incidence waves and chemical potential of graphene bilayer – the features that may be harnessed for varieties of applications that include switching, sensing in environmental monitoring and medical diagnostics, filtering and absorption of waves.

Acknowledgment

The authors would like to thank two anonymous reviewers for the fruitful suggestions to improve the status of manuscript.

References

- [1] A. Ebrahimi, W. Withayachumnankul, S. Al-Sarawi, and D. Abbott, "High-sensitivity metamaterial-inspired sensor for microfluidic dielectric characterization," *IEEE Sensors J.*, vol. 14, no. 5, pp. 1345–1351, May 2014.
- [2] J. Y. Rhee, Y. J. Yoo, K. W. Kim, Y. J. Kim, and Y. P. Lee, "Metamaterials based perfect absorbers," *J. Electromagn. Waves Appl.*, vol. 28, pp. 1541–1580, 2014.

- [3] E. Gazzola, A. Pozzato, G. Ruffato, E. Sovrnigo, and A. Sonato, "High-throughput fabrication and calibration of compact high-sensitivity plasmonic lab-on-chip for biosensing," *Optofluidics, Microfluidics Nanofluidics*, vol. 3, pp. 13–21, 2016.
- [4] M. Ghasemi, M. A. Baqir, and P. K. Choudhury, "On the metasurface based comb filters," *IEEE Photon. Technol. Lett.*, vol. 28, no. 10, pp. 1100–1103, May 2016.
- [5] M. A. Baqir and P. K. Choudhury, "Hyperbolic metamaterial-based UV absorber," *IEEE Photon. Technol. Lett.*, vol. 29, no. 18, pp. 1548–1551, Sep. 2017.
- [6] M. Baqir, A. Farmani, T. Fatima, M. Raza, S. Shaukat, and A. Mir, "Nanoscale, tunable, and highly sensitive biosensor utilizing hyperbolic metamaterials in the near-infrared range," *Appl. Opt.*, vol. 57, pp. 9447–9454, 2018.
- [7] S. Moghaddas, M. Ghasemi, P. K. Choudhury, and B. Y. Majlis, "Engineered metasurface of gold funnels for terahertz wave filtering," *Plasmonics*, vol. 13, pp. 1595–1601, 2018.
- [8] J. Chen *et al.*, "Engineering the magnetic plasmon resonances of metamaterials for high-quality sensing," *Opt. Exp.*, vol. 25, pp. 3675–3681, 2017.
- [9] J. Chen *et al.*, "Enhancing the magnetic plasmon resonance of three-dimensional optical metamaterials via strong coupling for high-sensitivity sensing," *J. Lightw. Technol.*, vol. 36, no. 16, pp. 3481–3485, Aug. 2018.
- [10] S. Zhang, D. A. Genov, Y. Wang, M. Liu, and X. Zhang, "Plasmon-induced transparency in metamaterials," *Phys. Rev. Lett.*, vol. 101, pp. 047401-1–047401-4, 2008.
- [11] M. Fleischhauer, A. Imamoglu, and J. P. Marangos, "Electromagnetically induced transparency: Optics in coherent media," *Rev. Modern Phys.*, vol. 77, pp. 633–673, 2005.
- [12] Z. Chai, X. Hu, Y. Zhu, S. Sun, H. Yang, and Q. Gong, "Ultracompact chip-integrated electromagnetically induced transparency in a single plasmonic composite nanocavity," *Adv. Opt. Mater.*, vol. 2, pp. 320–325, 2014.
- [13] H. Schmidt and A. Imamoglu, "Giant Kerr nonlinearities obtained by electromagnetically induced transparency," *Opt. Lett.*, vol. 21, pp. 1936–1938, 1996.
- [14] Y. Ling *et al.*, "Polarization-controlled dynamically switchable plasmon-induced transparency in plasmonic metamaterial," *Nanoscale*, vol. 10, pp. 19517–19523, 2018.
- [15] J. Gu *et al.*, "Active control of electromagnetically induced transparency analogue in terahertz metamaterials," *Nature Commun.*, vol. 3, pp. 1151-1–1151-6, 2012.
- [16] X. Zhou, X. Ling, H. Luo, and S. Wen, "Identifying graphene layers via spin hall effect of light," *Appl. Phys. Lett.*, vol. 101, pp. 251602-1–251602-4, 2012.
- [17] I. O. Zolotovskii, Y. S. Dadoenkova, S. G. Moiseev, A. S. Kadochkin, V. V. Svetukhin, and A. A. Fotiadi, "Plasmon-polariton distributed-feedback laser pumped by a fast drift current in graphene," *Phys. Rev. A*, vol. 97, pp. 053828-1–053828-6, 2018.
- [18] M. Ghorbanzadeh, S. Darbari, and M. Moravvej-Farshi, "Graphene-based plasmonic force switch," *Appl. Phys. Lett.*, vol. 108, pp. 111105-1–111105-5, 2016.
- [19] M. A. Baqir, P. K. Choudhury, T. Fatima, and A.-B. M. A. Ibrahim, "Graphene-over-graphite-based metamaterial structure as optical filter in the visible regime," *Optik*, vol. 180, pp. 832–839, 2019.
- [20] M. Ghasemi, P. K. Choudhury, and M. A. Baqir, "On the double nano-coned graphene metasurface-based multiband CIC absorber," *Plasmonics*, to be published. doi: [10.1007/s11468-019-00907-y](https://doi.org/10.1007/s11468-019-00907-y).
- [21] M. A. Baqir and P. K. Choudhury, "Graphene-based slab waveguide for slow-light propagation and mode filtering," *J. Electromagn. Waves Appl.*, vol. 31, pp. 2055–2063, 2017.
- [22] A. Farmani, A. Zarifkar, M. H. Sheikhi, and M. Miri, "Design of a tunable graphene plasmonic-on-white graphene switch at infrared range," *Superlattices Microstruct.*, vol. 112, pp. 404–414, 2017.
- [23] B. Zeng *et al.*, "Hybrid graphene metasurfaces for high-speed mid-infrared light modulation and single-pixel imaging," *Light: Sci. Appl.*, vol. 7, pp. 51-1–51-8, 2018.
- [24] K.-J. Yee, J.-H. Kim, M. H. Jung, B. H. Hong, and K.-J. Kong, "Ultrafast modulation of optical transitions in monolayer and multilayer graphene," *Carbon*, vol. 49, pp. 4781–4785, 2011.
- [25] X. Shi *et al.*, "Plasmonic analog of electromagnetically induced transparency in nanostructure graphene," *Opt. Exp.*, vol. 21, pp. 28438–28443, 2013.
- [26] X. He, F. Liu, F. Lin, and W. Shi, "Graphene patterns supported terahertz tunable plasmon induced transparency," *Opt. Exp.*, vol. 26, pp. 9931–9944, 2018.
- [27] X. Yan *et al.*, "Dynamically controllable plasmon induced transparency based on hybrid metal-graphene metamaterials," *Sci. Reps.*, vol. 7, 2017, Art. no. 13917.
- [28] Z. Vafapour and A. Zakery, "New regime of plasmonically induced transparency," *Plasmonics*, vol. 10, pp. 1809–1815, 2015.
- [29] S.-X. Xia, X. Zhai, L.-L. Wang, and S.-C. Wen, "Plasmonically induced transparency in double-layered graphene nanoribbons," *Photon. Res.*, vol. 6, pp. 692–702, 2018.
- [30] M. Qin, L. Wang, X. Zhai, Q. Lin, and S. Xia, "Multispectral plasmon induced transparency in a defective metasurface plasmonic nanostructure," *IEEE Photon. Technol. Lett.*, vol. 30, no. 11, pp. 1009–1012, Jun. 2018.
- [31] C. T. Riley, J. S. Smalley, J. R. Brodie, Y. Fainman, D. J. Sirbuly, and Z. Liu, "Near-perfect broadband absorption from hyperbolic metamaterial nanoparticles," *Proc. Nat. Acad. Sci. USA*, vol. 114, pp. 1264–1268, 2017.
- [32] S. Berthier and J. Lafait, "Effective medium theory: Mathematical determination of the physical solution for the dielectric constant," *Opt. Commun.*, vol. 33, pp. 303–306, 1980.
- [33] A. D. Rakić, A. B. Djurišić, J. M. Elazar, and M. L. Majewski, "Optical properties of metallic films for vertical-cavity optoelectronic devices," *Appl. Opt.*, vol. 37, pp. 5271–5283, 1998.
- [34] A. Vakil and N. Engheta, "Transformation optics using graphene," *Science*, vol. 332, pp. 1291–1294, 2011.
- [35] B. Zhao, J. Zhao, and Z. Zhang, "Enhancement of near-infrared absorption in graphene with metal gratings," *Appl. Phys. Lett.*, vol. 105, pp. 031905-1–031905-4, 2014.
- [36] S. Bellucci *et al.*, "Electrical permittivity and conductivity of a graphene nanoplatelet contact in the microwave range," *Materials*, vol. 11, pp. 2519-1–2519-11, 2018.